A carbon nanotube optical rectenna

Asha Sharma[‡], Virendra Singh[‡], Thomas L. Bougher[‡], and Baratunde A. Cola[*]

[*]Correspondence to: cola@gatech.edu
[‡]These authors contributed equally

This PDF file contains the methods with Supplementary Figures 1-13 and Supplementary Tables 1-2.

## 1. Turn-on voltage, field enhancement, effective barrier thickness, and asymmetry

Two different metal electrodes with different work functions were tested to correlate the effect of metal work function on rectification ratio and turn-on voltage. Several multiwall carbon nanotube-insulator-metal (MWNT-I-M) devices were fabricated in the same batch to produce similar array heights. These arrays were then coated with 8 nm of Al_2O_3 in the same atomic layer deposition (ALD) run. The turn-on voltage of MWNT-I-M devices with Ca (work function ~ 2.9 eV) and Al (work function ~ 4.3 eV) top metal electrodes was determined based on the experimental current-voltage curves. The turn-on voltage was defined as the voltage at which a line fit to a linear portion of the current-voltage curve intercepts the y-axis (that is, zero current, which is chosen to be 1 μA). This choice in definition of the turn-on voltage is arbitrary, so the main purpose of this analysis to create a self-consistent picture in which to compare the effects of work function on the onset of significant nonlinearity in our devices, and to estimate the extent of insulator barrier thinning due to geometric field enhancement. Supplementary Fig. 1 shows that the estimated turn-on voltage is 1.3 V smaller for Ca (0.3 V) top contact compared to Al (1.6 V).
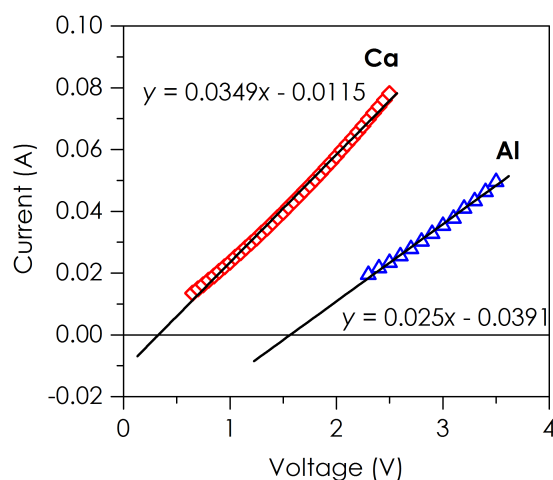
Supplementary Fig. 1. Determination of turn-on voltage from a linear portion of the measured current-voltage curves for MWNT-I-Ca and MWNT-I-Al devices.

To determine the effects of geometric field enhancement at MWNT tips on diode rectification and turn-on voltage, we tested planar Au-Al_2O_3-Ca diodes, which were fabricated to closely match the contrast in work function and oxide thickness in the MWNT-I-Ca devices for comparison. Planar M-I-M device geometries with glass/Ti/Au-Al_2O_3-Ca/Al were fabricated with various areas ranging from 0.01-0.04 cm^2 by first depositing Ti (30 nm)/Au (100 nm) on ultra-smooth glass substrates using e-beam evaporation. Then 8 nm of Al_2O_3 dielectric was deposited using ALD. Current-voltage characteristics measured on the planar devices with different active areas are shown in Supplementary Fig. 2. The planar devices produced rectification ratios (~ 1.2 at ± 2.75 V d.c. bias) and tunnel currents (~ 1.5 μA/cm^2 at 2.75 V) that are several orders of magnitude lower than the currents produced in the MWNT-I-Ca diodes

(Fig. 2b). These results suggests that reduced effective barrier resistance due to geometric field enhancement could contribute significantly to the much higher tunnel currents and asymmetry achieved in the MWNT-I-M diodes. A simple energy level diagram is shown in Fig. 2a to illustrate the potential effects of work function contrast and field enhancement on the resistance to electron tunneling in MWNT-I-M devices. Since the field enhancement is only expected in the forward direction, it contributes to unidirectional thinning of the tunneling barrier. This is because a single diode can be viewed roughly as a MWNT point contact emitter against a planar surface (Fig. 1a).
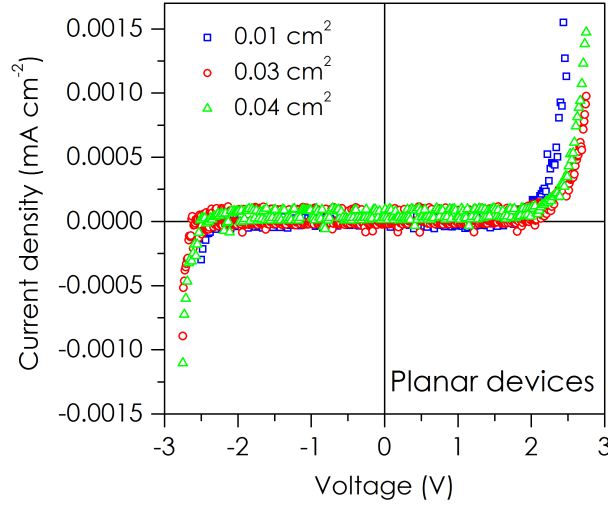
Supplementary Fig. 2. Current-voltage characteristics of planar M-I-M devices with glass/Ti/Au-Al$_2$O$_3$-Ca/Al structure with an active area of 0.01 cm^2, 0.03 cm^2, and 0.04 cm^2.

The electron tunneling equations from Simmons[1] are often used to fit experimental data for M-I-M diodes, however it has been shown that while these equations predict the behavior of planar structures qualitatively, the current density is often under-predicted significantly.[2,3] The current-voltage curves of carbon nanotube devices often differs somewhat from the exponential relationship between current and voltage in previous studies,[4] which is consistent with the observation in the MWNT device data in this work. Understanding the limitations of this theory, the Simmons equations were used with the experimentally estimated turn-on voltages to determine the effective barrier thickness of an equivalent planar structure that would produce a current at these voltages. More recent work has developed numerical solutions to electron tunneling through insulators,[5-7] however the original analytical expressions using the WKB approximation are sufficient to examine the qualitative current-voltage behavior of planar devices.[8] The equivalent planar structures were used because carbon nanotube diode data does not fit well to classic tunneling theory because of effects including variation of curvature and electron density of states at carbon nanotube tips.[9,10] The equation for the current density under a forward applied bias for dissimilar electrodes separated by a dielectric barrier is given by Simmons:[11]

$$J = J_o \left\{ \overline{\varphi} \exp\left(-A\overline{\varphi}^{\frac{1}{2}}\right) - \left(\overline{\varphi} + eV\right) \exp\left[-A\left(\overline{\varphi} + eV\right)^{\frac{1}{2}}\right] \right\}$$

(1)

where, $J_o = \dfrac{e}{2\pi h \Delta s^2}$, and $A = \dfrac{4\pi \Delta s \sqrt{2m}}{h}$, $\overline{\varphi}$ is the average potential barrier height with respect to electrode Fermi level, V is the applied voltage, Δs is the barrier thickness, m is electron mass, h is Plank's constant, and e is the electronic charge.[11] When the image force potential is considered the effective work function is given as:

$$\overline{\varphi} = \varphi_2 - \left[\frac{s_1 + s_2}{2s}\left(eV + \Delta\varphi\right)\right] - \frac{1.15\lambda s}{\Delta s}\ln\left[\frac{s_2(s - s_1)}{s_1(s - s_2)}\right]$$

(2)

Where λ and s_1 are given by:

$$\lambda = \frac{e^2 \ln 2}{16\pi\varepsilon\varepsilon_o s}$$

(3)

$$s_1 = 1.2\lambda s / \varphi_2$$

(4)

It should be noted that the expression for λ used here is a factor of 2 smaller than the original Simmons equation, which was in error as noted by Miskovsky et al.[7] For intermediate voltages $(eV > \varphi_1)$ s_2 is:

$$s_2 = s - \frac{9.2\lambda s}{3\varphi_2 + 4\lambda - 2\left(eV + \Delta\varphi\right)} + s_1$$

(5)

and for high voltages $(eV > \varphi_1)$:

$$s_2 = \frac{\left(\varphi_2 - 5.6\lambda\right)s}{eV + \Delta\varphi}$$

(6)

ε is the dielectric constant of the insulator, and its value is taken to be 5.1 as determined from the measured capacitance values for 8 nm thin ALD deposited Al_2O_3 barrier on planar surface (see section 3 below). s is the barrier thickness and $\Delta s = s_2 - s_1$ and $\Delta\varphi = \varphi_2 - \varphi_1$. The barrier height at the metallic electrode is the difference between the electrode work function and the electron affinity of the oxide barrier. The barrier height, $\varphi_1 = 1.9$ eV for Ca, $\varphi_1 = 3.3$ eV for Al, and $\varphi_2 = 4.1$ eV for MWNT was taken in the above expressions. All parameters in the current density equation were held constant except for the barrier thickness. A threshold current of 1 µA was set and the effective barrier thickness that would produce the threshold current was calculated. The area used for the current calculation was the projected device area (0.01 cm^2) multiplied by the fill fraction of the MWNTs (0.005) for an effective area of 5×10^{-5} cm^2. Because the two devices were identical except for the work function of the metal electrode, it was expected that the difference between the work function of Ca and Al could account for the difference in turn-on voltages that was observed experimentally. Since the deposited barrier thickness was the same in both devices, it is expected that the modeled effective barrier thickness of each device would also be the same. The physical barrier thickness of the device is 8 nm, but this does not account for the electron tunneling enhancement produced by the concentrated electric field at the tips of the MWNTs. The effective electron tunneling barrier thickness (s_{eff}) was determined to be approximately 1.5 nm for both Ca and Al. These are the barrier thickness in a planar device that would produce 1 µA of current at the respective turn-on voltages. A plot of the theoretical current-voltage for Ca and Al planar devices with the aforementioned barrier thickness are shown in Supplementary Fig. 3. This result provided confirmation that the difference in work

function of the two top metals was responsible for the change in turn-on voltage between the two device types.
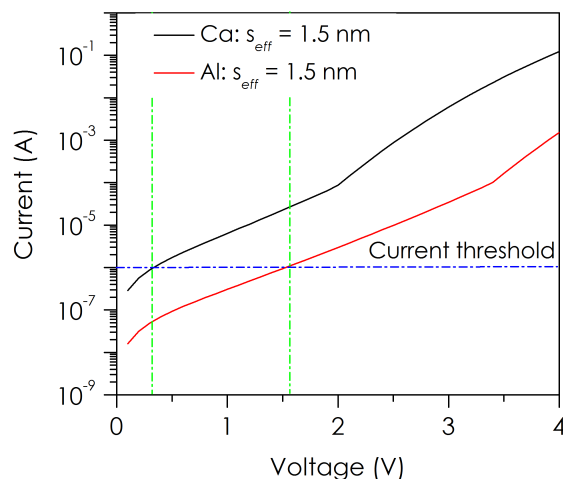
Supplementary Fig. 3. Theoretical current-voltage characteristics and estimated effective barrier thicknesses (s_{eff}) based on an equivalent planar MWNT-I-Ca and MWNT-I-Al structures (that is, the same material properties were used) that would produce a magnitude of current similar to experimentally observed currents at the turn-on voltages (0.3 and 1.6 V for Ca and Al, respectively). The arbitrary current threshold that defines voltage turn on is 1 μA.

The current-voltage curves for the planar devices (Au-Al$_2$O$_3$-Ca) were fitted using the above Simmons' theoretical electron tunneling equations by fitting for the effective barrier thickness, s_{eff}. This application of Simmons' equations is also similar to previous work that changed the barrier thickness to fit the model.[8] The data and best-fit theoretical curves are shown in Supplementary Fig. 4 with the experimentally measured data. It can be seen that the theoretical fittings agree well with the measured current-voltage curves for three different devices. The s_{eff} in the planar Au-Al$_2$O$_3$-Ca diodes is estimated to be 2.8 nm from fitting Simmons' theory to three devices with different areas (0.01 cm^2, 0.03 cm^2, 0.04 cm^2) as shown in Supplementary Fig. 4. The Au and Al$_2$O$_3$ layers were measured with atomic force microscopy to be atomically smooth (rms roughness of 0.52 ± 0.06 and 0.64 ± 0.02 nm, respectively); therefore, it is unlikely that surface roughness contributes to field enhancement in the planar diodes, as has been observed in prior work.[8] The fact that the effective barrier thickness is thinner than the physical barrier thickness means that the tunneling equations under predict the current density, which is consistent with previous findings.[8,12] The nearly twofold reduction in s_{eff} for MWNT-I-M diodes compared to the equivalent planar structures presents strong evidence that field enhancement at MWNT tips contributes to effective barrier thinning in these devices. However, the effective device field enhancement is expected to be less than that of a single carbon nanotube because of collective screening of the external field by neighboring tubes in the array.[13]
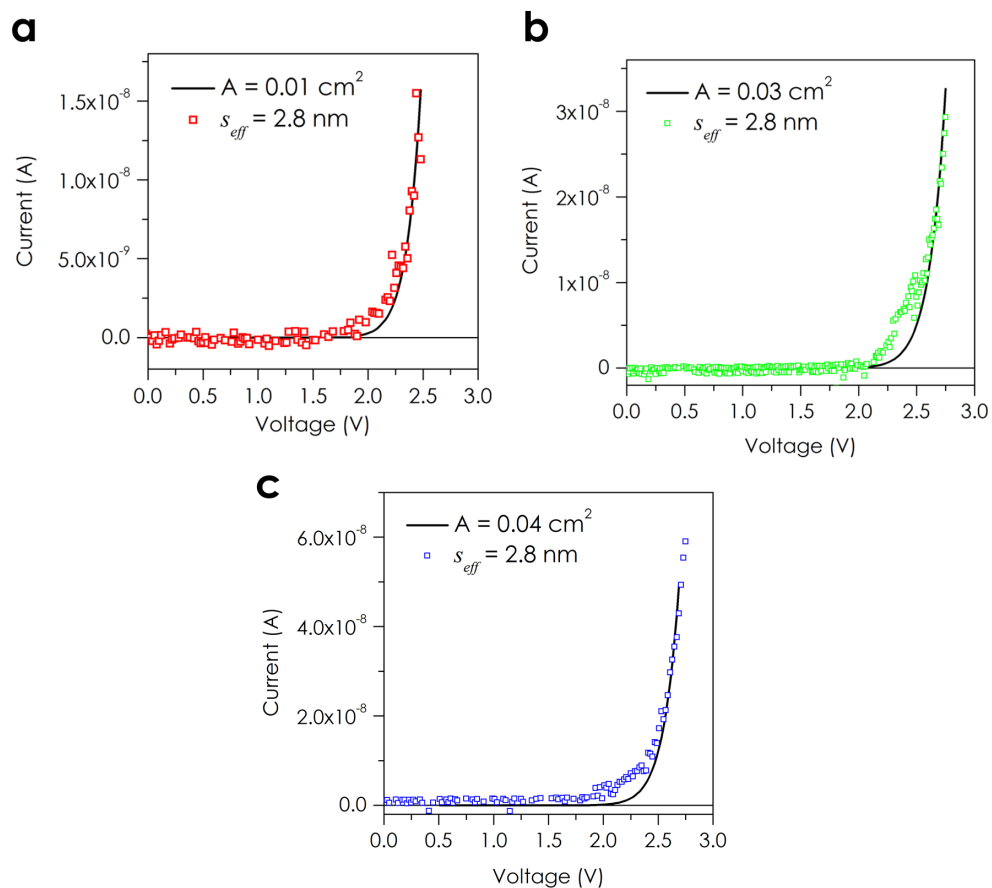
Supplementary Fig. 4. The fitted curves and experimental data for three different planar devices with different active area, (a) 0.01 cm², (b) 0.02 cm², (c) 0.04 cm².
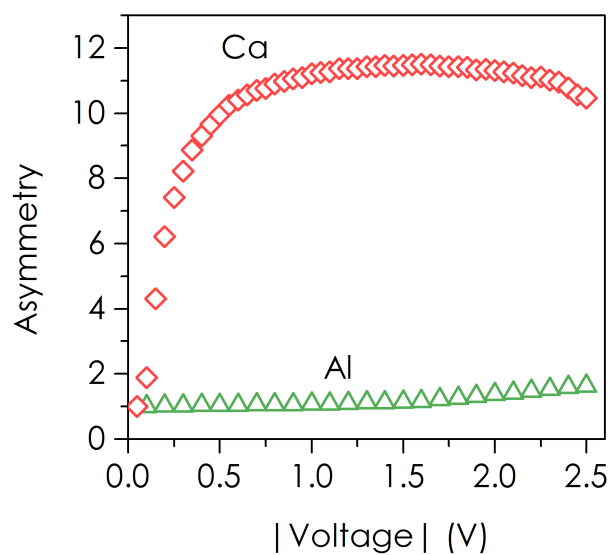

Supplementary Fig. 5. Electrical asymmetry (A) of Ca and Al devices in Fig. 2b where $A = |I(V)/I(-V)|$.

2. Effect of MWNT work function on electrical performance

Different carbon nanotube growth conditions or substrates can produce MWNT structures with different morphology and can result in different electrical properties and work functions.[14] The work functions of MWNTs grown on Si substrates with different resistivities were measured by Kelvin probe on three different spots on the same sample and on MWNTs grown in different batches (Supplementary Fig. 6a). The MWNTs that were grown on medium resistivity Si substrates (0.01-0.05 Ω.cm) exhibited a higher work function (5 eV) than the work function of MWNTs that were grown on low resistivity Si (0.001-0.005 Ω.cm), which was 4.8 eV. The MWNTs with 5 eV work function were used in the devices in the main text.

In order to correlate the diode current rectification with the bottom MWNT electrode work function, Al_2O_3 was deposited on the two MWNT samples followed by the deposition of a Ca top metal electrode. The inset in Supplementary Fig. 6a indicates clearly that the rectification in the current for a given applied d.c. bias is higher in devices that use MWNTs with a higher work function. These results were reproducible on several devices as shown in Supplementary Fig. 6. Evaluation of the samples in scanning electron microscope (SEM) revealed that the MWNTs that were grown on low resistivity substrates were less straight in comparison to the MWNTs that were grown on medium resistivity substrates (Supplementary Figs. 6b and 6c). The higher degree of carbon nanotube waviness could explain the lower work functions measured on the MWNTs grown on low resistivity Si substrates because such waviness could increase defects, entanglement, and as a result cause a substantial decrease in the electrical conductivity of the MWNTs.[15]
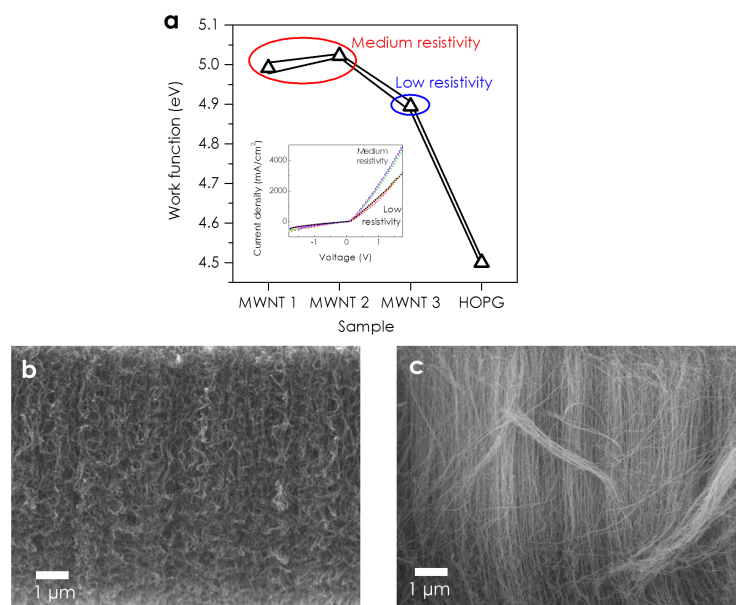
Supplementary Fig. 6. Effect of MWNT work function (WF) on current-voltage characteristics. (a) WF of the MWNTs grown on medium resistivity and low resistivity Si substrates. WF of highly ordered pyrolytic graphite (HOPG) is shown to compare. The inset shows current-voltage characteristics of the devices fabricated using the low WF, and high WF MWNTs as the bottom electrode in the diode structure. (b) SEM image of MWNT arrays on low resistivity (0.001-0.005 Ω.cm) Si substrate. (c) SEM image of MWNT arrays on medium resistivity (0.01-0.05 Ω.cm) Si substrate.

3. Capacitance measurements of MWNT-O-M diode arrays

The measured capacitances (C) based on the apparent device area (0.1 cm^2) of MWNT-I-M diode arrays with different oxide thicknesses (Fig. 2c) were nearly constant in a standard low frequency range (up to 10^6 Hz). The results do not show the inverse thickness relation of a conventional parallel plate capacitor because the permittivity of nanoscale oxide insulators can decrease with thickness.[16] For the MWNT-O-M arrays fabricated with 8 nm Al$_2$O$_3$, specific capacitance of approximately 3.4 µF/cm^2 or roughly 2 attofarads per MWNT junction, and a dielectric constant (ε) of 3.8 can be extracted using the following expression

$$C = C_1 + C_2 + C_3 \ldots\ldots\ldots = n\left(\frac{\varepsilon_0 \varepsilon A}{d}\right).$$

(7)

The measured capacitance is 1.7 nF for an 8 nm oxide (Fig. 2c). The measured MWNT diameter is approximately 8 nm, so the area of a MWNT tip = π x 4^2 x 10^{-14} cm^2 = 50.24 x 10^{-14} cm^2. Based on the number density of MWNTs estimated from SEM images, there are approximately 10^9 MWNTs in an area of 0.1 cm^2. Therefore, the actual area A = 50.24 x 10^{-14} cm^2 x 10^9 = 50.24 x 10^{-5} cm^2. Hence, the specific capacitance C/A = 1.75 nF/50.24 x 10^{-5} cm^2 = 0.0338 x 10^{-4} F/cm^2 = 3.38 x 10^{-6} F/cm^2 = 3.38 µF/cm^2. The dielectric constant (ε) of 3.8 can be extracted from the calculated specific capacitance for 8 nm oxide by using the equation,

$$\varepsilon = \left(C/A\right) \times \frac{d}{\varepsilon_0}.$$

(8)

Similarly, the capacitance per junction can be evaluated by dividing the measured capacitance (1.7 nF) by the number of MWNTs in an area of 0.1 cm^2 (10^9 MWNT). Hence, the capacitance per junction is 1.7 nF/10^9, which is 1.7 x 10^{-18} F.

The measured capacitances (at 1 kHz and 20 mV$_{rms}$) of the planar Au-Al$_2$O$_3$-Ca devices with 8 nm of oxide as a function of area (ranging from 0.01-0.04 cm^2) are shown in Supplementary Fig. 7. The capacitance per unit area (C/A) as extracted from the linear fit of the slope of capacitance versus area curve is 569 nF/cm^2. Using the value of C/A in a conventional parallel plate capacitor model where capacitance is given by equation (8), a dielectric constant (ε) of 5.14 is calculated for the ALD deposited 8 nm Al$_2$O$_3$.
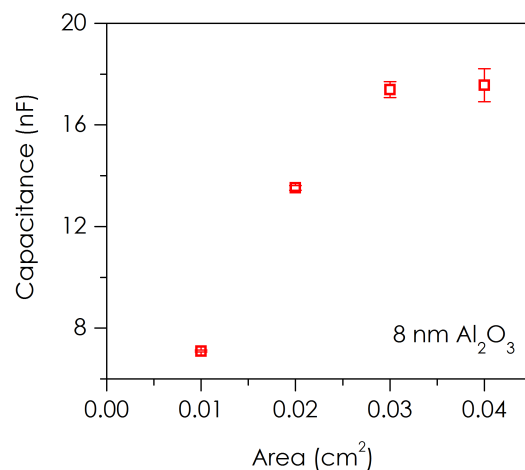
Supplementary Fig. 7. Measured capacitance of planar Au-Al$_2$O$_3$-Ca (8 nm oxide) structures as a function of area, at 1 kHz and ac amplitude of 20 mV$_{rms}$.

4. Device consistency and reliability
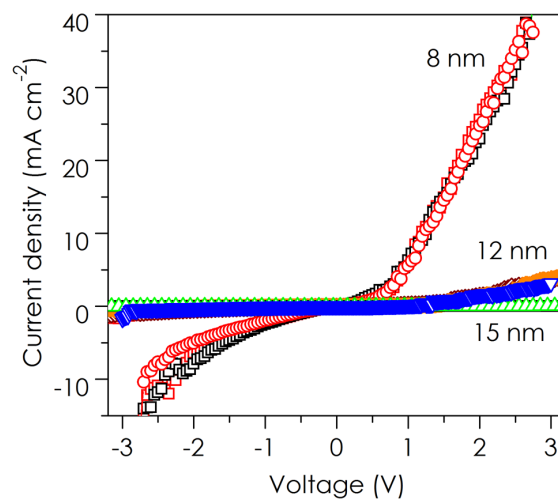
Supplementary Fig. 8. Carbon nanotube-insulator-metal tunnel diode characteristics. The current-voltage characteristics of the tunnel diodes using 8, 12, and 15 nm of Al$_2$O$_3$. Multiple repeat scans are shown for each data set to demonstrate consistency.
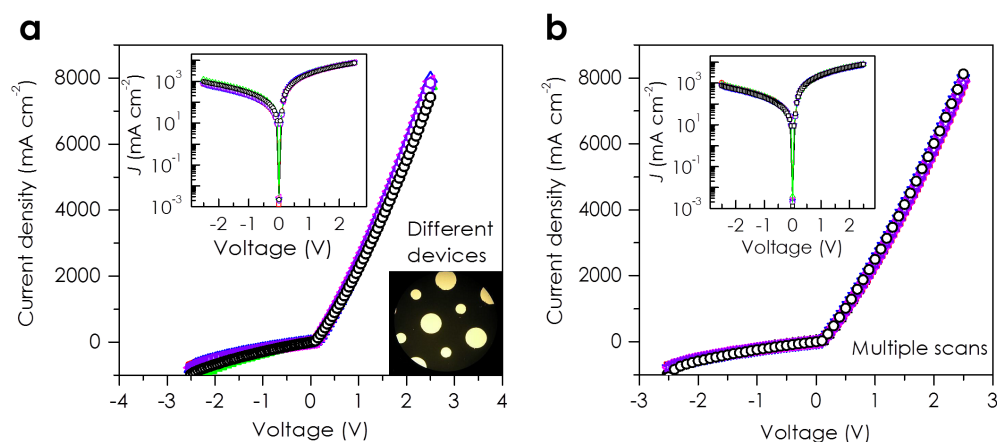
Supplementary Fig. 9. (a) Current-voltage characteristics of the fabricated MWNT-I-Ca diodes measured on six devices with an active area of 0.01 cm^2 (the picture shows an optical image of the devices with two different top contact areas). (b) Current-voltage characteristics of a device showing excellent electrical stability during multiple scans. The insets in (a) and (b) show semi-logarithmic plots of the data.

5. Optical rectification photoresponse
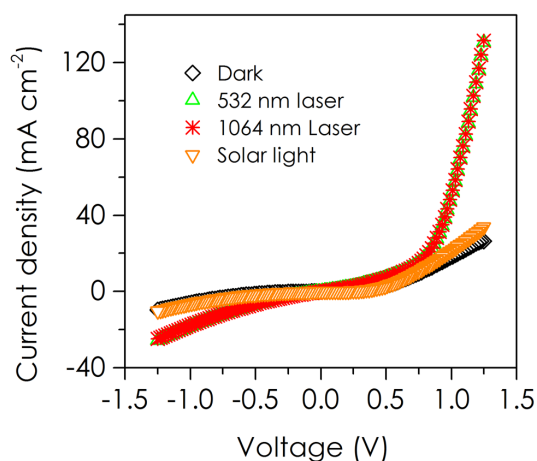
Supplementary Fig. 10. Optical rectification of infrared, visible, and simulated solar light (data for devices in Fig. 3). **a**, Current-voltage characteristics of device responding to 1.5 AM solar (100 mW cm^{-2}), 1064 nm (92 mW cm^{-2}), and 532 nm (26 mW cm^{-2}) illumination with 10% transmission through the top metal contact.

Classically, rectification can be identified from examining the nonlinearity of diode conductance,[17] where the amplitude of a small applied a.c. voltage bias, $V_{ac}\cos(\omega t)$, can be

related to the rectified d.c. current as[18] $I \approx [I(V_{dc}) + 1/2\,(\beta/R)V_{ac}^2]$, where $\beta = 1/2\,(\partial^2 I/\partial V^2)/(\partial I/\partial V)$ is the diode responsivity and $R = 1/(\partial I/\partial V)$ is the diode differential resistance. However, when a nanoscale junction is illuminated with radiation of energy $\hbar\omega$, the plasmonic response of the junction produces an a.c. voltage, V_{opt}, at frequency ω across the junction, and, in the limit of small a.c. amplitudes ($eV_{opt} \ll \hbar\omega$), a quantum correction is required to consider photon-assisted tunneling.[19] In this semi-classical picture,[19] the diode differential resistance is

$$R_{qc} = \frac{(2\hbar\omega/e)}{[I(V_{dc}+\hbar\omega/e)-I(V_{dc}-\hbar\omega/e)]}, \qquad (9)$$

and the diode responsivity is

$$\beta_{qc} = \frac{e}{\hbar\omega}\frac{[I(V_{dc}+\hbar\omega/e)-2I(V_{dc})+I(V_{dc}-\hbar\omega/e)]}{[I(V_{dc}+\hbar\omega/e)-I(V_{dc}-\hbar\omega/e)]}, \qquad (10)$$

where $R = R_{qc}$, $\beta = \beta_{qc}$, and $V_{opt} = V_{ac}$ as $\hbar\omega \to 0$. At $V_{dc} = 0$, $R_{qc} = 70$ ohm-cm^2 and $\beta_{qc} = 0.4$ V^{-1} for 1064 nm illumination (Fig. 3a), and these results are consistent with the values in Supplementary Table 1, which are based on applying a classical treatment to the illuminated $I(V_{dc})$ curve (Supplementary Fig. 11). The semi-classical rectified d.c. current can be expressed as $I = [I(V_{dc}) + 1/2\,(\beta_{qc}/R_{qc})V_{opt}^2]$, and the semi-classical rectified d.c. diode voltage as $V_D = -1/2\,\beta_{qc}V_{opt}^2$, which is valid when the rectenna is operating below its cutoff frequency.[20] Power generation, P_{out}, can be expressed as one-half the open-circuit voltage (V_{oc}) times one-half the short-circuit current (I_{sc}), which, in terms of basic device parameters is

$$P_{out} = -\beta_{qc}^2 V_{opt}^4/16R_{qc}, \qquad (11)$$

where β_{qc} and R_{qc} are at zero-bias conditions ($V_{dc} = 0$). The maximum responsivity and optical voltage at unity quantum efficiency[19] are $e/\hbar\omega$ and $\hbar\omega/e$, respectively, which reduces equation (11) to $P_{out} = -(\hbar\omega/e)^2/16R_{qc}$.

Supplementary Table 1. Dark and illuminated diode characteristics, measured open-circuit voltage and short-circuit current, and estimated energy conversion efficiencies for the devices in Fig. 3 of the main text. The statistical uncertainty in the extracted diode characteristics is approximately ±10% and approximately ±5% in the measured voltage and current. The illuminated diode resistance and responsivity are based on applying a classical treatment to the illuminated $I(V_{dc})$ curve – the illuminated $I(V_{dc})$ curve is shifted in this case such that $I = 0$ at $V_{dc} = 0$. While this approach is only an approximation, it is useful when the range of voltages tested for dark $I(V_{dc})$ characteristics is less than $\pm\hbar\omega$, and we find the agreement with equations (9) and (10) at $V_{dc} = 0$ to be within ±30%.

| Device	Dark		Illuminated		Measured V_{oc} (mV)	Measured I_{sc} (mA cm^{-2})	Estimated conversion efficiency (%)
	Zero bias resistance (kohm cm²)	Zero bias responsivity (V^{-1})	Zero bias resistance (kohm cm²)	Zero bias responsivity (V^{-1})			
1064 nm laser (Figure 3b)	7.5	9	0.08	0.3	-0.69	6.5*10^{-3}	10^{-5}
532 nm laser (Figure 3c)	7.5	9	0.07	0.3	-0.16	1.7*10^{-3}	3*10^{-6}
AM 1.5 solar (Figure 3d)	5.1	4.1	5.7	0.4	-0.58	3.0*10^{-4}	4*10^{-7}
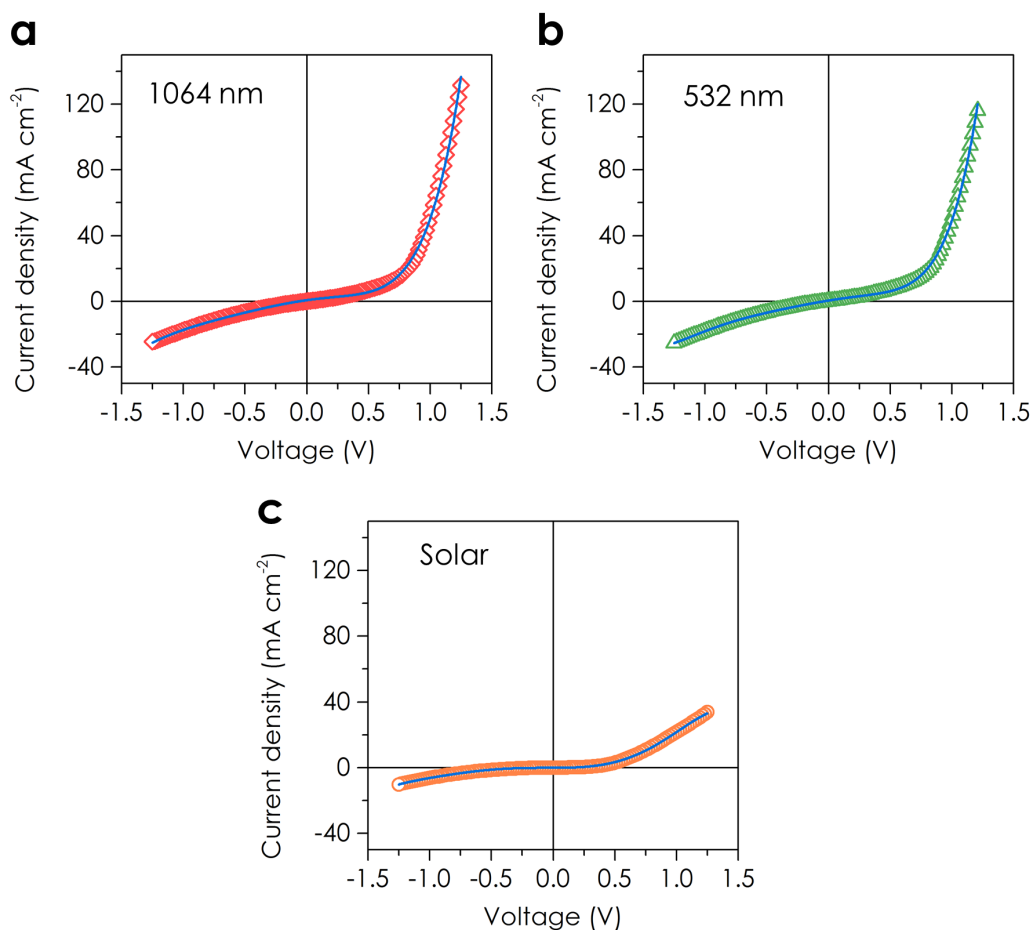
Supplementary Fig. 11. Illuminated current-voltage response, corrected such that $I = 0$ at $V_{dc} = 0$, for (a) 1064 nm, (b) 532 nm, and (c) 1.5 AM solar illumination. These are the same devices as those in Fig. 3. The black curve is a 6th-order polynomial fit to the data that is used to compute the differential resistance and responsivity as an approximation to the semi-classical response.

Supplementary Table 2. Comparison to previous reports of optical rectification in metal-vacuum-metal (MVM) junctions. Results from this work reported for 532 nm light with 8 nm oxide device with Ca top metal.

Authors	Year	Pressure	Junction	Max Current at Zero Bias (A)	Incident Power (W/cm²)	Ratio Current to Laser Intensity (A-cm²/W)
Nguyen et. al.[21]	1989	Vacuum	MVM	2.0E-09	20	1.00E-10
Miskovsky et. al.[7]	2010	Vacuum	MVM	1.0E-13	0.13	7.85E-13
Ward et. al.[18]	2010	Vacuum	MVM	9.0E-09	22600	3.98E-13
Bragas et. al.[22]	1998	Vacuum	MVM	3.0E-12	30	1.00E-13
This work	2015	1 atm	MIM	1.0E-05	0.092	1.09E-04

6. Thermoelectric response
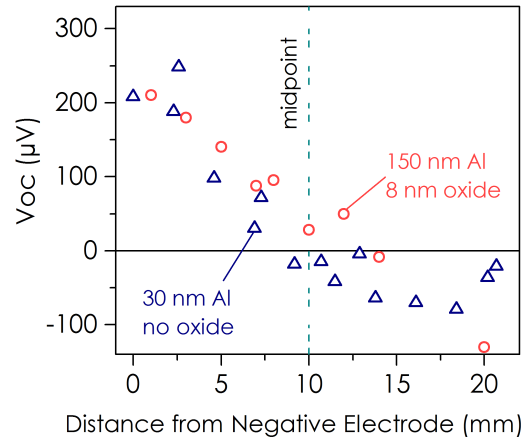
Supplementary Fig. 12. Thermoelectric voltage vs. distance from the negative probe for a typical MWNT-I-M rectenna with 150 nm Al capping layer to absorb all thermal energy at the surface. The sample is heated at 11.2 W/cm^2 532 nm laser intensity, which is about 112 times more intense than the maximum illumination intensity in our rectenna response tests. Also shown is a device with a semi-transparent 30 nm top Al metal and no oxide layer. The red dashed line is the background voltage level. The halfway point between the positive and negative probe is approximately 10 μm from the negative probe.

7. Additional evidence for optical rectification
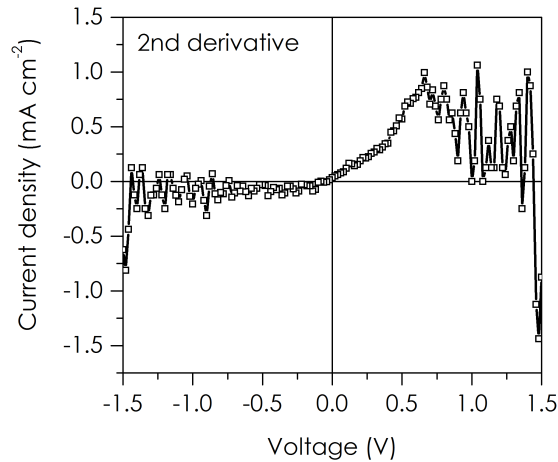
Supplementary Fig. 13. MWNT rectenna device under 1.5 AM solar illumination. The 2nd derivative is computed from a 6th-order polynomial fit to the illuminated current-voltage curve (from Supplementary Fig. 11c) to approximate the semi-classical correction. The agreement in the shape and sign of the voltage where the 2nd derivative of the current-voltage crosses the abscissa with the data in Supplementary Fig. 11c is evidence for the photoresponse originating from optical rectification.[18]

References

1   Castrucci, P. *et al.* Light harvesting with multiwall carbon nanotube/silicon heterojunctions. *Nanotechnology* **22**, 115701 (2011).
2   Park, B., Kim, Y. J., Graham, S. & Reichmanis, E. Change in Electronic States in the Accumulation Layer at Interfaces in a Poly(3-hexylthiophene) Field-Effect Transistor and the Impact of Encapsulation. *ACS Appl. Mater. Inter.* **3**, 3545-3551 (2011).
3   Luo, J., Zhu, J., Huang, Z. & Zhang, L. Arrays of Ni nanowire/multiwalled carbon nanotube/amorphous carbon nanotube heterojunctions containing Schottky contacts. *Appl. Phys. Lett.* **90**, 033114 (2007).
4   Xiao, K. *et al.* Photoelectrical characteristics of a C/CNx multiwalled nanotube. *Adv. Func. Mater.* **17**, 2842-2846 (2007).
5   Ghatak, A. K., Thyagarajan, K. & Shenoy, M. R. Novel numerical technique for solving the one-dimensional Schroedinger equation using matrix approach - application to quantum well structures. *IEEE J. Quantum Elect.* **24**, 1524-1531 (1988).
6   Hashem, I. E., Rafat, N. H. & Soliman, E. A. Theoretical study of metal-insulator-metal tunneling diode figures of merit. *IEEE J. Quantum Elect.* **49**, 72-79 (2013).
7   Miskovsky, N. M., Cutler, P. H., Feuchtwang, T. E. & Lucas, A. A. The multiple-image interactions and the mean-barrier approximation in MOM and MVM tunneling junctions. *Appl. Phys. A* **27**, 139-147 (1982).
8   Cowell, E. W. *et al.* Advancing MIM electronics: amorphous metal electrodes. *Adv. Mater.* **23**, 74-78 (2011).
9   Buldum, A. & Lu, J. P. Electron Field Emission Properties of Closed Carbon Nanotubes. *Phys. Rev. Lett.* **91**, 236801 (2003).
10   Bonard, J.-M., Kind, H., Stockli, T. & Nilsson, L.-O. Field emission from carbon nanotubes: The first five years. *Solid State Electron.* **45**, 893-914 (2001).
11   Simmons, J. G. Electric tunnel effect between dissimilar electrodes separated by a thin insulating film. *J. Appl. Phys.* **34**, 2581-2590 (1963).
12   Krishnan, S., Stefanakos, E. & Bhansali, S. Effects of dielectric thickness and contact area on current–voltage characteristics of thin film metal–insulator–metal diodes. *Thin Solid Films* **516**, 2244-2250 (2008).
13   Mayer, A., Miskovsky, N. M., Cutler, P. H. & Lambin, P. Transfer-matrix simulations of field emission from bundles of open and closed (5,5) carbon nanotubes. *Phys. Rev. B* **68**, 235401 (2003).
14   Su, W. S., Leung, T. C., Bin, L. & Chan, C. T. Work function of small radius carbon nanotubes and their bundles. *Appl. Phys. Lett.* **90**, 163103-163101 (2007).
15   Dai, H. J., Wong, E. W. & Lieber, C. M. Probing electrical transport in nanomaterials: Conductivity of individual carbon nanotubes. *Science* **272**, 523-526 (1996).
16   de Jonge, N., Lamy, Y., Schoots, K. & Oosterkamp, T. H. High brightness electron beam from a multi-walled carbon nanotube. *Nature* **420**, 393-395 (2002).
17   Tu, X. W., Lee, J. H. & Ho, W. Atomic-scale rectification at microwave frequency. *J. Chem. Phys.* **124**, 021105 (2006).
18   Ward, D. R., Huser, F., Pauly, F., Cuevas, J. C. & Natelson, D. Optical rectification and field enhancement in a plasmonic nanogap. *Nat. Nanotechnol.* **5**, 732-736, (2010).
19   Sachit, G., Saumil, J. & Garret, M. Quantum theory of operation for rectenna solar cells. *J. Phys. D Appl. Phys.* **46**, 135106 (2013).
20   Sanchez, A., Davis, J. C. F., Liu, K. C. & Javan, A. The MOM tunneling diode: Theoretical estimate of its performance at microwave and infrared frequencies. *J. Appl. Phys.* **49**, 5270-5277 (1978).
21   Nguyen, H. Q. *et al.* Mechanisms of Current Rectification in an STM Tunnel Junction and the Measurement of an Operational Tunneling Time. *IEEE T. Electron Dev.* **36**, 2671-2678 (1989).
22   Bragas, A. V., Landi, S. M. & Martinez, O. E. Laser field enhancement at the scanning tunneling microscope junction measured by optical rectification. *Appl. Phys. Lett.* **72**, 2075-2077 (1998).